On the stability of Taylor bubbles inside a confined highly porous medium

Marion Serres [a,b], Marie-Line Zanota [b], Régis Philippe [b], Valérie Vidal [a,*]

[a] Laboratoire de Physique, CNRS UMR 5672, École Normale Supérieure de Lyon, Université de Lyon, 46 Allée d'Italie, 69007 Lyon, France
[b] Laboratoire de Génie des Procédés Catalytiques, CNRS UMR 5285, CPE Lyon, Université de Lyon, 43 boulevard du 11 novembre 1918, 69100 Villeurbanne, France

A B S T R A C T

This work focuses on the local hydrodynamics of a multiphase gas–liquid flow forced into an innovative medium of high porosity (96%): an open cell solid foam. The gas (nitrogen) and liquid (ethanol) phases are injected at constant flow-rates in a millichannel to form a well-controlled Taylor flow which enters the porous medium. Based on a fluorescence technique, the apparent liquid holdup in the porous medium is quantified, and its evolution in time and along the porous medium extracted from spatiotemporal diagrams. The analysis of the main frequency, when varying the gas–liquid flow-rate ratio, leads to the identification of two hydrodynamic regimes. A model based on a scaling analysis is proposed to quantify the dimensionless numbers describing the transition between both regimes. It points out that the bubble length fixed by the Taylor flow is the control parameter. The model prediction of the critical bubble length at which the transition occurs is in good agreement with the experimental observations.

© 2016 Elsevier Ltd. All rights reserved.

1. Introduction

Gas–liquid (G–L) flows inside porous media are encountered in many different areas. On the one hand, in geosciences, various processes require the fine comprehension of multiphase flows inside the underground. For instance, the optimization of air sparging processes for water decontamination or ground remediation (Reddy and Adams, 2001; Semer et al., 1998), the prediction of viscous fingering in enhanced oil recovery (Babchin et al., 2008), the comprehension and the prediction of CO_2 becoming during its storage by injection inside saline aquifers (Eccles et al., 2009) or by deep deposit of liquid CO_2 on the ocean floor (Kang et al., 2005) can be mentioned among many examples. Natural phenomena like gas migration or gas plume generation in oceanic sediments also involve G–L flows in a porous medium. Their study is of interest for the understanding of seismic micro-events generation and earthquake prediction (Tary et al., 2012), or in the framework of potential new energy resources (Chazallon et al., 2009; Gay et al., 2007). On the other hand, the chemical industry also involves a large number of reactive and nonreactive processes where a two-phase gas–liquid flow and a solid porous medium are involved. In the specific field of heterogeneous catalysis, for instance, a gas often

has to react with a liquid medium in presence of an active solid catalyst. Different reactor configurations (packed beds, slurry bubble columns, stirred tanks, fluidized beds, etc.) have been setup to optimize the solid handling, mixing performance, heat, mass and momentum transfers to the chemical reaction constraints. Many studies have focused on the global performance of such reactors, providing quantification of the liquid holdup and mass transfer for given reactor geometries and porous media (see for example Hessel et al. (2005); Losey et al. (2001); Marquez et al. (2008)). However, due to the strong hydrodynamic coupling between the different phases motion, in addition to their mixing and reaction, a precise knowledge of the flow patterns is still necessary.

The hydrodynamics of multiphase flows in porous media have been widely studied in the case of granular materials. Most of the previous works aimed at identifying the governing parameters of the flow, to infer fluid-induced structures from the hydrodynamics or to predict the gas extrusion rate of a plume in the case of sediments (Mazzini et al., 2008; Mörz et al., 2007; Nermoen et al., 2010). These systems have been investigated under different geometry, confinement or driving forces, for packed (rigid porous) beds (Geistlinger et al., 2006; 2009) or unpacked (mobile) beds (Holtzman and Juanes, 2010; Holtzman et al., 2012; Kong et al., 2009). Hence, buoyancy-driven multiphase flows have been thoroughly described for gas injection at constant flow rate (Sandnes et al., 2011; Varas et al., 2013, 2015) or constant pressure (Eriksen et al., 2015). However, most of these studies focused on model

---

* Corresponding author.
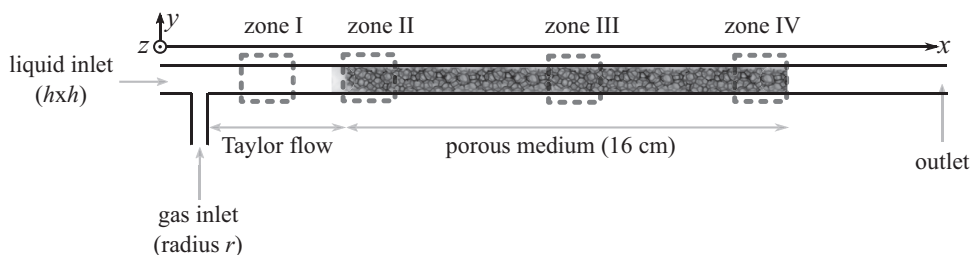 *E-mail address:* valerie.vidal@ens-lyon.fr (V. Vidal).

Fig. 1. Top view of the experimental cell. A regular, segmented gas–liquid flow (Taylor flow) is injected at the entrance of a porous medium (open cell solid foam) in a millichannel of 2 mm × 2 mm square cross-section and total length 24 cm. Direct observation is performed over four different zones, upstream (zone I), at the entrance of the medium (zone II), inside the foam (zone III) and at the exit of the porous medium (zone IV).

granular media such as spherical glass beads, which may exhibit properties far from the porous media encountered as sediments or catalytic components.

In the general context of process intensification (Stankiewicz and Moulijn, 2000), the chemical engineering research was directed toward new multiphase catalytic reactors presenting possible multiscale morphologies like monoliths, open cell foams or mini-packed beds to face market pressure and satisfy an increased environmental consideration (Hessel et al., 2005). Open cell solid foams (OCSF) reactors present a great potential because of their high porosity and contact area. They were first studied and developed to optimize continuous gas–solid reactors and heat exchangers due to the drastic reduction in pressure loss while maintaining an attractive contact surface for reaction (Twigg and Richardson, 2007). Stemmet et al. (2008, 2005, 2006) were the first ones to propose their use as a catalyst support in a three-phase reactor with interesting performances and pioneering chemical engineering characterizations. In the meantime, Topin et al. (2006) developed the use of OCSF for boiling heat transfer and characterized the flow and pressure drop inside this medium. Recently, Tourvielle et al. (2015a, b) were the first to implement OCSF in a millichannel in order to benefit from the combination of the excellent mass and heat transfers observed in mini-packed beds (Losey et al., 2001) with a low pressure drop due to the intrinsic properties of this original porous medium. They demonstrated the interest of such combination for the chemical engineering industry, and pointed out the particular hydrodynamics induced by the confinement in this unusual porous medium. However, the hydrodynamics of a gas–liquid flow crossing an open cell solid foam in a confined geometry has not yet been characterized.

In this work, we investigate the hydrodynamic regimes of a confined segmented gas–liquid flow crossing an open cell solid foam in a horizontal square channel. The G–L flow is obtained by injecting gas and liquid at constant flow-rates at the inlet of the experimental device. To answer the need of optimization and prediction of transfer and mixing properties, we focus on direct observations of the G–L flow before and inside the solid foam and describe the different flow patterns. A frequency analysis of the apparent liquid holdup signal is performed to infer the governing parameter of the multiphase flow.

2. Experimental setup

2.1. Description

The cell consists of a square channel of $h = 2$ mm width (cross-section $h \times h = 4$ mm^2) and total length 24 cm (Fig. 1), drilled in PEEK (polyether ether ketone), a solid thermoplastic polymer often used for its strong mechanical and chemical resistance. The top wall is replaced by a glass plate to allow direct visualization. To ensure the same surface properties of the walls inside the channel,

Table 1
Density ρ and viscosity μ of the liquid (ethanol) and gas (nitrogen) phases.

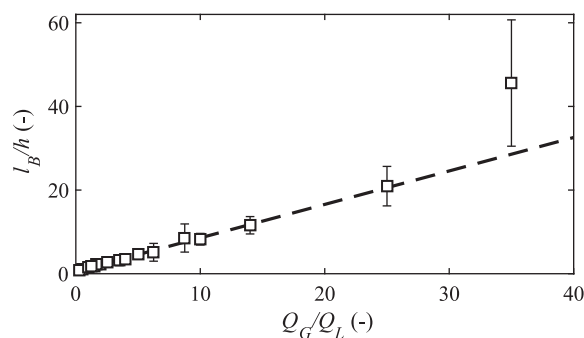|	ρ (kg/m^3)	μ (Pa s)
Ethanol (L)	795	1.15×10^{-3}
Nitrogen (G)	1.25	1.76×10^{-5}

Fig. 2. Bubble length l_B, normalized with the channel width h, as a function of the gas over liquid flow-rate Q_G/Q_L [white squares, experimental data; dashed black line, fit from Eq. (5), $l_B/h \simeq Q_G/Q_L$].

a thin (10 nm) layer of diamond-like carbon is coated by plasma deposition. The porous medium (open cell solid foam, described in Section 2.2) occupies the whole section of the channel, over a length of 16 cm. The liquid (ethanol) is injected directly at the entrance of the millichannel (liquid inlet, Fig. 1) at constant flow-rate Q_L, while the gas (nitrogen) is injected perpendicularly, at constant flow-rate Q_G, through a circular inlet of radius $r = 0.5$ mm (T-junction). The physical properties (density and viscosity) of the liquid and gas phases are given in Table 1. The ethanol–nitrogen surface tension is $\sigma \simeq 22$ mN/m at room temperature (Dittmar et al., 2003).

The liquid and gas flow-rates vary in the range $Q_L = [0.5–8]$ cm^3/min and $Q_G = [2–35]$ cm^3/min, and we explore values of the gas over liquid flow-rate ratio $Q_G/Q_L = [0.25–35]$. These experimental conditions ensure a regular segmented flow, also called 'Taylor flow', where bubbles occupying the whole cross-section of the channel alternate periodically with liquid slugs (Angeli and Gavriilidis, 2008; Garstecki et al., 2006). The gas bubble length at the entrance of the solid foam vary between 2 and 91 mm (Fig. 2).

2.2. Solid foam as a porous medium

The porous medium under study is an open cell solid foam made of vitreous carbon (80 PPI, ERG Aerospace). The morphological characteristics of this porous medium is roughly provided by the manufacturer (pore density in Pore Per Inch, here 80 PPI). To
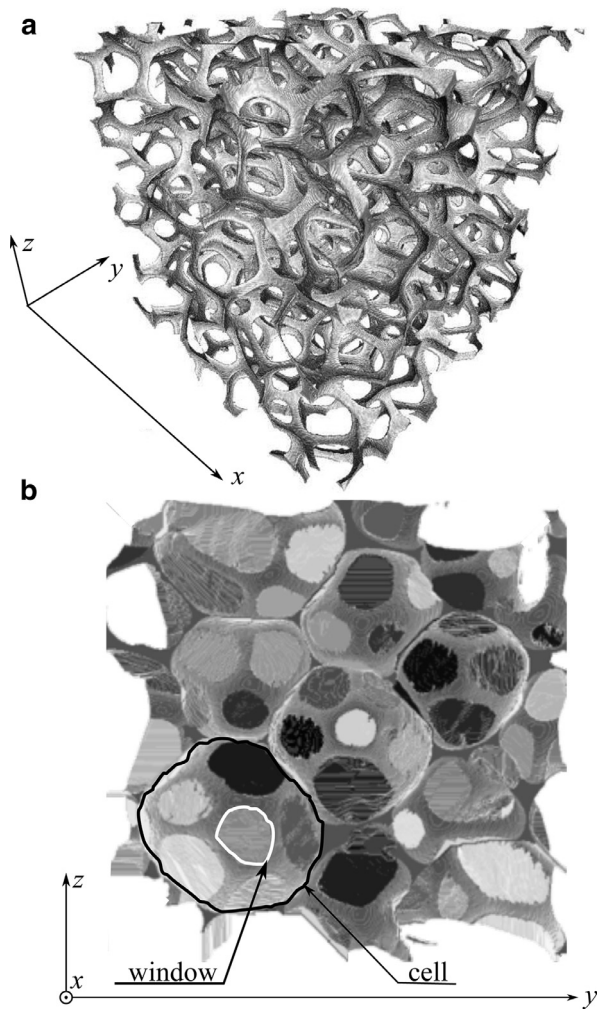
a

b

Fig. 3. X-ray tomography analysis of a $3 \times 3 \times 3$ mm³ block of the open cell solid foam used in the experiments (vitreous carbon 80PPI, ERG Aerospace). (a) 3D image of the foam solid structure (struts). (b) Windows and cells contours in a front view $(y - z)$ of the foam. The subunits are materialized by different gray shades. Two examples are underlined by a black (cell) or white (window) contour (black arrows).
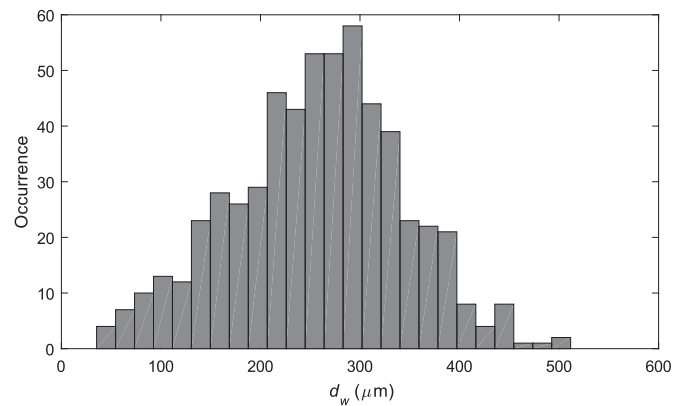

Fig. 4. Distribution of the window size, d_w, computed from the X-ray tomography images (578 windows analyzed). The distribution gives the typical window diameter, $d_w = 257 \pm 85$ µm.

Table 2
Mean and standard deviation of the struts (d_s), windows (d_w) and cells (d_c) diameter, and porosity ϕ [solid foam 80PPI, ERG Aerospace].

		Mean	Standard deviation
Struts	d_s	55 µm	23 µm
Windows	d_w	257 µm	85 µm
Cells	d_c	604 µm	86 µm
Foam porosity	ϕ	96%	0.3%

get details on the structure of this material, it has been characterized by X-ray tomography (GE Phoenix v|tome|x s, RX tube of 160 kV with focal point of up to 1 µ m) with a spatial resolution of 5 µm. The data analysis is performed with iMorph® software (Brun et al., 2008) which gives access to the 3D image of the foam (Fig. 3a). The solid structure is composed by the struts (Fig. 3a) and the void fraction can be divided into two subunits, namely cells and windows. The cells correspond to the void cages enclosed by the struts, while the windows consist of the junction between two cells (Fig. 3).

The subunits size is quantified with iMorph® software, which approximates each subunit either by a sphere (cell) or by a thin elliptic cylinder (window). The windows are the smaller void subunits, and therefore are the ones which most constrain the flow inside the solid foam. Their thickness corresponds to the struts diameter. In average, we consider that the dimension which most constrain the gas–liquid flow is its elliptic face smaller axis, d_w, hereafter referred to as the windows typical diameter. The distribution of d_w is shown in Fig. 4. The average struts (d_s), windows (d_w) and cells (d_c) diameters is displayed in Table 2. The foam porosity is computed, and equal to $\phi = 96 \pm 0.3\%$ (Table 2).

2.3. Images acquisition and analysis

Direct observation of the flow patterns is performed in four zones of the experimental cell (Fig. 1): upstream in the Taylor flow region (zone I), at the entrance of the porous medium (zone II), inside the foam (zone III) and at the outlet of the porous medium (zone IV). For each zone, a movie of total duration of 15–20 s is acquired with a camera (Solinocam H2D2, at 113 fps) mounted on a fluorescence microscope (Olympus BX51M). A fluorescent dye (Rhodamine 6B) is previously dissolved inside the liquid phase (ethanol), so that this latter appears bright on the image, while the gas phase (nitrogen) appears in black (Fig. 5a).

Image analysis is then performed with Matlab (Mathworks®) to quantify the liquid holdup, ϵ_L, defined as the volume fraction of liquid inside a given observation zone. First, the image sequence is divided by a reference image, where the liquid phase entirely fills the open cell solid foam (Fig. 5b). Then, the images are binarized by fixing a threshold of 0.9 to separate the gas (<0.9) and liquid (≥0.9) phases. Each image is thus a matrix containing either 1 (solid foam or liquid phase) or 0 (gas phase). The gas fraction ϵ_G is then estimated as the number of pixels occupied by the gas phase, divided by the total number of pixels in the frame. The liquid holdup is finally computed as $\epsilon_L = \phi - \epsilon_G$. Note that ϵ_L is an *apparent liquid holdup*. Indeed, it corresponds to the volume fraction of liquid of a 3D cell, computed from a 2D observation. This method leads to an overestimation of the solid phase, which induces an underestimation of the real liquid holdup. However, due to the high foam porosity ($\phi = 96\%$) and the small depth of the millichannel (2 mm), the gas phase can be detected even if a small gas bubble is located at the channel bottom, far from the observation wall (Fig. 5a). In addition, this study is mainly based on the frequency analysis of the liquid pulses, which is captured by this method, although the liquid holdup amplitude is not exactly quantified.
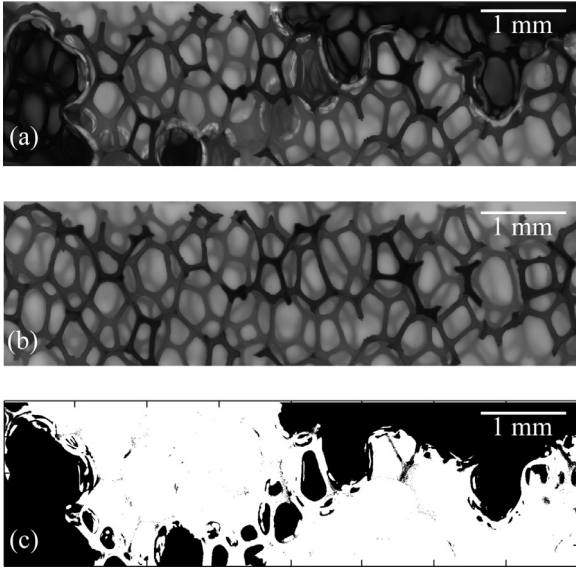
Fig. 5. (a) Raw image from data acquisition. The fluorescence technique makes it possible to distinguish the liquid phase (bright) and the gas phase (dark), superimposed to the foam solid structure (struts). (b) Reference image where the liquid entirely fills the foam. (c) Binarization of image (a), obtained by dividing the raw image (a) by the reference (b) and using a threshold of 0.9 (see text).

3. Different hydrodynamic regimes

The temporal evolution of the apparent liquid holdup ϵ_L inside the four different zones is displayed in Fig. 6 [(a–d) and (e–h), upper panels] for two examples of gas over liquid flow-rate ratio, $Q_G/Q_L = 0.25$ [Fig. 6a–d, upper panels] and $Q_G/Q_L = 3.5$ [Fig. 6e–h, upper panels]. The pulses due to the successive passages of the liquid slugs from the initial Taylor flow are clearly visible. To analyze the signal frequency content and the flow disorganization after entering the solid foam, the frequency content of the signal is computed by a Fourier transform over a moving temporal window. Spatiotemporal diagrams are thus represented in Fig. 6 (a- and c–h, lower panels), and make it possible to follow the frequency content both in space (zones I–IV) and time.

In the Taylor flow region, upstream the porous medium (zone I), the main frequency f_0 of the periodic Taylor flow regime is clearly recovered, sometimes with higher frequencies corresponding to the harmonics [Fig. 6a, lower panel]. Two regimes can be inferred from the examples presented in Fig. 6. On the one hand, at low Q_G/Q_L, the frequency content is almost unchanged when entering the porous medium (Fig. 6a–b, lower panel), although the amplitude of the apparent liquid holdup can strongly vary (Fig. 6a–b, upper panel). After some distance inside the porous medium the harmonics disappear (Fig. 6c) but the main frequency still remains, although it becomes more and more noisy (Fig. 6d). On the other hand, at high Q_G/Q_L, the initial Taylor frequency is lost as soon as the gas–liquid flow enters the solid foam (Fig. 6f). Interestingly, in some cases, we report a feedback of the flow disorganization at the porous medium entrance (zone II) on the upstream Taylor flow (zone I). For $Q_G/Q_L = 3.5$, for instance, the low-frequency modulation generated at the entrance of the solid foam couples to the higher Taylor flow main frequency, and disorganizes partly the upstream flow (see the modified frequency content for $t > 5$ s, Fig. 6e, lower panel).

Note that the mean value of the apparent liquid holdup, $\langle\epsilon_L\rangle$, varies along the porous medium, from zone II to zone IV. The increasing trend of $\langle\epsilon_L\rangle$ inside the foam (zone II and III) is observed for all ratio Q_G/Q_L (Fig. 6b, c and f, g). In most experiments, $\langle\epsilon_L\rangle$ decreases at the foam exit (zone IV), except for high values

of Q_G/Q_L. Although the existence of a slip between the gas and liquid phases is a common feature in two-phase flows propagating inside an empty channel (Hanratty, 2013) or a porous medium (Garcia Maldonado et al., 2008; Iliuta et al., 1998), no link has been evidenced with a continuous change of the liquid holdup along the flow propagation direction. Only few experimental works have pointed out a variation of the liquid holdup along different porous media in the case of vertical, counter-current gas–liquid flows (Aferka et al., 2011; Calvo et al., 2009). However, the authors considered only instantaneous values of ϵ_L, and not a time average as in our experiments, which prevents any quantitative comparison. Moreover, let us remind that $\langle\epsilon_L\rangle$ here is inferred from direct visualization at the wall and is therefore the time average of an *apparent* liquid holdup. Although this latter may be different from the real liquid holdup, its variations can be qualitatively discussed. In our experiments, the increase of $\langle\epsilon_L\rangle$ along the channel may be related to the establishment distance of a stationary regime when the two-phase flow enters the solid foam. Further experiments would be necessary to quantify the real liquid holdup and its variations along the porous medium.

The next sections focus on the disorganization of the periodic Taylor flow (zone I) at the entrance of the porous medium (zone II). In particular, we aim at describing the transition between the first hydrodynamic regime, hereafter named '*Taylor-like regime*', for which the flow frequency is almost not affected when entering the foam, and the second hydrodynamic regime, hereafter named '*modulated regime*', for which the apparent liquid holdup exhibits a low-frequency modulation right at the porous medium entrance.

4. Scaling model

In this section, we develop a theoretical argument based on a scaling analysis to describe the transition between the 'Taylor-like regime' and the 'modulated regime' described in Section 3. Based on experimental observations, the first hint for a quantitative criterion lies in the fact that the gas bubbles entering the porous medium are able to propagate as a whole, or fragment when pushed through the solid porous structure.

On the one hand, we consider the Taylor flow upstream the porous medium (zone I in Fig. 1 and left part of Fig. 7). Previous studies have demonstrated that the dimensionless number controlling the hydrodynamics of a gas–liquid flow in a microchannel is the ratio of the Reynolds numbers associated with each phase (Kreutzer et al., 2005; Völkel, 2009):

$$\frac{Re_G}{Re_L} = \left(\frac{\rho_G\,\mu_L}{\rho_L\,\mu_G}\right)\frac{Q_G}{Q_L} \tag{1}$$

with $Re_G = \rho_G Q_G/\mu_G h$ and $Re_L = \rho_L Q_L/\mu_L h$, where μ and ρ denote the density and viscosity (see Table 1) and (G, L) the gas and liquid phase, respectively.

When entering the porous medium (Fig. 7), the bubble has to make its way through orifices smaller than the channel. In Section 2.2, we described two different subunits composing the void fraction of the solid foam: windows and cells. These latter can be seen as 'cages' surrounded by windows (see Fig. 3). As the smaller void subunits, the windows are the ones which constrain most the flow propagation and in particular, the possible bubble fragmentation. The dimensionless number controlling the bubble fragmentation corresponds to the balance between inertial forces, pushing the bubble forward, and surface tension, which tends to keep the bubble as a whole. This balance can be written as the two-phase Weber number, often used as the control parameter for bubbles or drops breakup when flowing through orifices (Galinat et al., 2005; Nambiar et al., 1992; Percy and Sleicher, 1983):

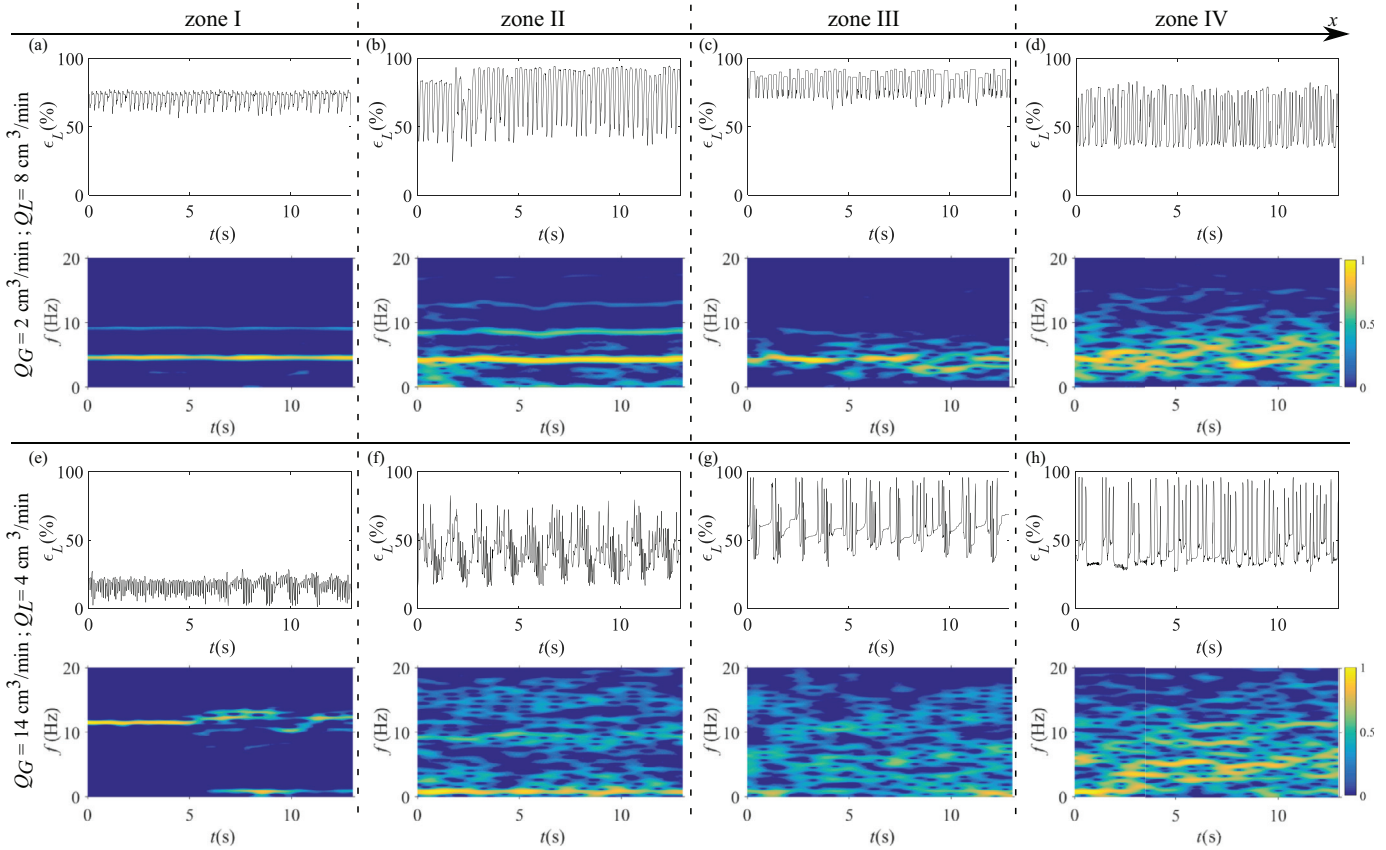$$We = \frac{\rho_L(Q_G + Q_L)^2 d_w}{(n_w S_w)^2 \sigma} \tag{2}$$

Fig. 6. (Color online) Spatiotemporal behavior of the apparent liquid holdup ϵ_L upstream and inside the porous medium for two different sets of gas and liquid flow-rates [(a–d) $Q_G = 2$ cm³/min, $Q_L = 8$ cm³/min, $Q_G/Q_L = 0.25$; (e-h) $Q_G = 14$ cm³/min, $Q_L = 4$ cm³/min, $Q_G/Q_L = 3.5$]. (Upper panels) Temporal evolution of the apparent liquid holdup ϵ_L in zones I–IV. (Lower panels) Spatiotemporal diagrams of the signal $\epsilon_L(t)$ frequency content [probability density function, color scale from 0 to 1]. Note the signature of the periodic liquid pulses in the Taylor flow (zone I), and the progressive flow disorganization after entering the porous medium.
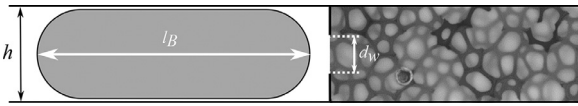

Fig. 7. Simplified model of a bubble entering the porous medium. The Taylor bubble (length l_B), occupying most of the millichannel square cross-section ($h \times h$), meets n_w windows of typical diameter d_w when entering the solid foam.

Table 3
Typical surface S_w of the windows (pores) and their number in a cross-section $h \times h$ of the millichannel, based on X-ray tomography analysis.

	Mean	Min	Max
S_w (mm²)	0.080	0.036	0.126
n_w	5	3	7

where d_w is the typical window diameter (see Table 2), S_w their typical area and n_w the average number of windows met by the bubble at the porous medium entrance, in a plane perpendicular to the flow propagation.

To account for both the characteristics of the Taylor flow entering the porous medium, and the condition for bubble fragmentation, we propose the following modified Weber number:

$$We' = \left(\frac{Re_G}{Re_L}\right) We \tag{3}$$

which combines the Reynolds numbers of the single phases entering the porous medium and the multiphase Weber number inside the solid foam,

$$We' = \left(\frac{\rho_G}{\sigma}\right)\left(\frac{\mu_L}{\mu_G}\right)\left(\frac{Q_G}{Q_L}\right)\left(\frac{Q_G + Q_L}{n_w S_w}\right)^2 d_w. \tag{4}$$

The average windows surface, S_w, and the number of windows n_w on a millichannel cross-section $h \times h$ are estimated from the X-ray tomography images (iMorph® software, Brun et al. (2008)) and displayed in Table 3. In spite of the dispersion inherent to the foam structure, we find, in average, $n_w \simeq 5$ and $S_w \simeq 0.08$ mm². Note that n_w is much smaller than the apparent number of win-

dows which can be seen on Fig. 3b. Due to perspective in Fig. 3b, many apparent windows are visible and overestimate the number of windows met by a bubble at the foam entrance. Indeed, most of them are at depth, located on cells sides or bottom, and should not be counted in the estimation of n_w. This latter was performed on a thin cross-section of the foam only, with a typical thickness equal to the struts size, $d_s = 55 \pm 23$ μm (Table 2).

Fig. 8 displays the main frequency f_0 of the temporal evolution of the apparent liquid holdup ϵ_L in zone I (Taylor flow, white squares) and zone II (entrance of the porous medium, black circles) as a function of We'. For $We' < 1$, the flow at the entrance of the solid foam keeps the Taylor flow main frequency (*Taylor-like regime*). For $We' > 1$, the flow disorganizes and the main frequency in the porous medium exhibits a lower frequency, modulating the signal (*modulated regime*). This figure, which exhibits a clear distinction between both regimes, validates the modified Weber number We' as the transition criterion for the flow regimes. In the next section, we interpret the transition criterion, $We' \simeq 1$, in terms of a critical bubble length above which the Taylor bubbles fragment when entering the porous medium, leading to the flow disorganization.
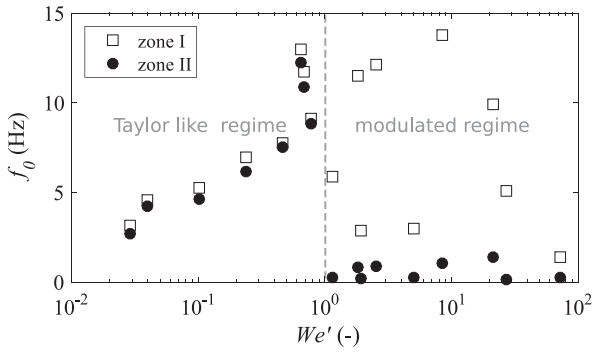
Fig. 8. Main frequency f_0 of the apparent liquid holdup signal as a function of the transition criterion, *We'*, defined as a modified Weber number [□ Taylor flow region (zone I); • entrance of the porous medium (zone II)].
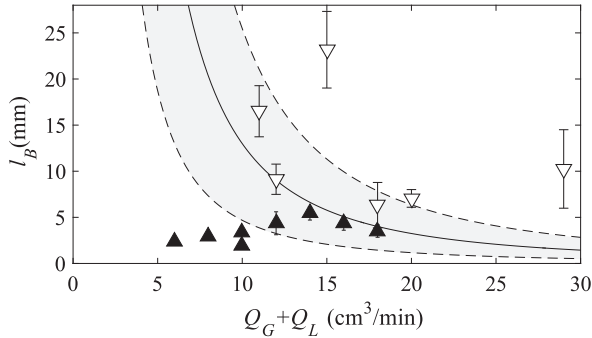

Fig. 9. Bubble length l_B in the Taylor flow upstream the porous medium (zone I) as a function of $(Q_G + Q_L)$. The symbols represent the two hydrodynamic regimes observed at the solid foam entrance [(▲, Taylor-like regime); (▽, modulated regime)]. The solid black line represents the critical bubble length l_B^* predicted by the model (Eq. (7)), and the light gray region accounts for the variation of the foam morphological parameters in the critical bubble length prediction.

5. Critical bubble length

The literature (Garstecki et al., 2006; Leclerc et al., 2010; van Steijn et al., 2007; Völkel, 2009) and the experiments presented in this work (Fig. 2) reveal a linear dependency between the length l_B of the bubbles in the segmented flow (Taylor flow) and the gas over liquid flow rate ratio, Q_G/Q_L:

$$\frac{l_B}{h} = \alpha \frac{Q_G}{Q_L} \tag{5}$$

with $\alpha \simeq 1$ (Fig. 2). Note that the point for the highest flow-rate ratio ($Q_G/Q_L = 35$) is not taken into account for the linear fit. Indeed, in this case, we report a departure from the well-defined Taylor flow. Replacing Q_G/Q_L in Eq. (4) leads to

$$We' = \left(\frac{\rho_G}{\sigma}\right)\left(\frac{\mu_L}{\mu_G}\right)\left(\frac{l_B}{h}\right)\left(\frac{Q_G + Q_L}{n_w S_w}\right)^2 d_w \tag{6}$$

This model therefore predicts a critical bubble length l_B^* above which the bubble fragmentation leads to the flow disorganization:

$$l_B^* = \left(\frac{\sigma}{\rho_G}\right)\left(\frac{\mu_G}{\mu_L}\right)\left(\frac{n_w S_w}{Q_G + Q_L}\right)^2\left(\frac{h}{d_w}\right) \tag{7}$$

Fig. 9 displays the critical bubble length, l_B^*, as a function of $(Q_G + Q_L)$. The range of critical bubble length predicted by the model (gray zone, Fig. 9) is computed by using the values of n_w and S_w presented in Table 3. Experimental measurements of the bubble length performed in the Taylor flow region (zone I) are reported, and the symbol indicates that the subsequent flow at the entrance of the solid foam (zone II) is either in the Taylor-like regime (black

triangles) or in the modulated regime (white triangles). The model and the prediction of the transition zone is in good agreement with the experimental observations.

6. Conclusion

We have investigated the hydrodynamics of a segmented gas–liquid flow entering a solid foam in a horizontal, square millichannel. The high porosity ($\sim$96%) of such porous medium gives rise to two different hydrodynamic regimes, which are characterized by quantifying the spatiotemporal evolution of the apparent liquid holdup, ϵ_L, along the channel. In the Taylor-like regime, the main frequency of the segmented Taylor flow is kept at the entrance of the porous medium; in the modulated regime, the flow disorganizes immediately when entering the solid foam and a lower modulation frequency appears.

The scaling model, based on a modified Weber number accounting for the relative velocity of the gas and liquid phases, provides a critical bubble length l_B^* for the segmented flow. For $l_B > l_B^*$, the bubble fragments at the entrance of the foam, leading to the flow disorganization. Experimental measurements of the Taylor bubble length for the different hydrodynamic regimes validate the model prediction. The bubble length in the Taylor flow can therefore be considered as the control parameter of the hydrodynamics inside the open cell solid foam, and can be used to predict the flow.

In the Taylor-like regime, we report the flow progressive disorganization as a function of the distance inside the porous medium. The influence of this parameter, which is out of the scope of this study, shall be the topic of a future work.

References

Aferka, S., Viva, A., Brunazzi, E., Marchot, P., Crine, M., Toye, D., 2011. Tomographic measurement of liquid hold up and effective interfacial area distributions in a column packed with high performance structured packings. Chem. Eng. Sci 66, 3413–3422.

Angeli, P., Gavriilidis, A., 2008. Taylor flow in microchannels. In: Li, D. (Ed.), Encyclopedia of Microfluidics and Nanofluidics. Springer, US, pp. 1971–1976.

Babchin, A., Brailovsky, I., Gordon, P., Sivashinsky, G., 2008. Fingering instability in immiscible displacement. Phys. Rev. E 77, 026301.

Bourry, C., Chazallon, B., Charlou, J.L., Donval, J.P., Ruffine, L., Henry, P., Gely, L., Çagatay, M.N., Inan, S., Moreau, M., 2009. Free gas and gas hydrates from the sea of Marmara, Turkey. chemical and structural characterization. Chem. Geol. 264, 197–206.

Brun, E., Vicente, J., Topin, F., Occelli, R., 2008. From 3D imaging of structures to diffusive properties of anisotropic cellular materials. In: Continuum Models and Discrete Systems (CMDS 11). Les Presses de l'Ecole des Mines de Paris, pp. 423–428.

Calvo, S., Beugre, D., Crine, M., Léonard, A., Marchot, P., Toye, D., 2009. Phase distribution measurements in metallic foam packing using X-ray radiography and micro-tomography. Chem. Eng. Process. 48, 1030–1039.

Dittmar, D., Fredenhagen, A., Oei, S.B., Eggers, R., 2003. Interfacial tensions of ethanol–carbon dioxide and ethanol–nitrogen. dependence of the interfacial tension on the fluid density–prerequisites and physical reasoning. Chem. Eng. Sci 58, 1223–1233.

Eccles, J.K., Pratson, L., Newell, R.G., Jackson, R.B., 2009. Physical and economical potential of geological CO_2 storage in saline aquifers. Environ. Sci. Technol. 43, 1962–1969.

Eriksen, F.K., Toussaint, R., Måløy, K.J., Flekkøy, E.G., 2015. Invasion patterns during two-phase flow in deformable porous media. Front. Phys. 3, 81.

Galinat, S., Masbernat, O., Guiraud, P., Dalmazzone, C., Noik, C., 2005. Drop break-up in turbulent pipe flow downstream of a restriction. Chem. Eng. Sci. 60, 6511–6528.

Garcia Maldonado, J.G., Bastoul, D., Baig, S., Roustan, M., Hébrard, G., 2008. Effect of solid characteristics on hydrodynamic and mass transfer in a fixed bed reactor operating in co-current gas–liquid up flow. Chem. Eng. Process. 47, 1190–1200.

Garstecki, P., Fuerstman, M.J., Stone, H.A., Whitesides, G.M., 2006. Formation of droplets and bubbles in a microfluidic T-junction-scaling and mechanism of break-up. Lab. Chip 6, 437–446.

Gay, A., Lopez, M., Berndt, C., Séranne, M., 2007. Geological controls on focused fluid flow associated with seafloor seeps in the lower Congo basin. Mar. Geol. 244, 68–92.

Geistlinger, H., Krauss, G., Lazik, D., Luckner, L., 2006. Direct gas injection into saturated glass beads: transition from incoherent to coherent gas flow pattern. Water Resour. Res. 42, W07403.

Geistlinger, H., Lazik, D., Krauss, G., Vogel, H.-J., 2009. Pore-scale and continuum modeling of gas flow pattern obtained by high-resolution optical bench-scale experiments. Water Resour. Res. 42, W04423.

Hanratty, T.J., 2013. Physics of Gas–Liquid Flows. Cambridge University Press, p. 354.

Hessel, V., Angeli, P., Gavriilidis, A., Löwe, H., 2005. Gas–liquid and gas–liquid–solid microstructured reactors: contacting principles and applications. Ind. Eng. Chem. Res. 44, 9750–9769.

Holtzman, R., Juanes, R., 2010. Crossover from fingering to fracturing in deformable disordered media. Phys. Rev. E 82, 046305.

Holtzman, R., Szulczewski, M.L., Juanes, R., 2012. Capillary fracturing in granular media. Phys. Rev. Lett. 108, 264504.

Iliuta, I., Larachi, F., Grandjean, B.P.A., 1998. Pressure drop and liquid holdup in trickle flow reactors: improved Ergun constants and slip correlations for the slit model. Ind. Eng. Chem. Res. 37, 4542–4550.

Kang, Q., Tsimpanogiannis, I.N., Zhang, D., Lichtner, P.C., 2005. Numerical modeling of pore-scale phenomena during CO_2 sequestration in oceanic sediments. Fuel Process. Technol. 86, 1647–1665.

Kong, X.-Z., Kinzelbach, W., Stauffer, F., 2009. Migration of air channels: an instability of air flow in mobile saturated porous media. Chem. Eng. Sci. 64, 1528–1535.

Kreutzer, M.T., Kapteijn, F., Moulijn, J.A., Heiszwolf, J.J., 2005. Multiphase monolith reactors: chemical reaction engineering of segmented flow in microchannels. Chem. Eng. Sci. 60, 5895–5916.

Leclerc, A., Philippe, R., Houzelot, V., Schweich, D., de Bellefon, C., 2010. Gas–liquid Taylor flow in square micro-channels: new inlet geometries and interfacial area tuning. Chem. Eng. J. 165, 290–300.

Losey, M.W., Schmidt, M.A., Jensen, K.F., 2001. Microfabricated multiphase packed-bed reactors: characterization of mass transfer and reactions. Ind. Eng. Chem. Res. 40, 2555–2562.

Marquez, N., Casta no, P., Makkee, M., Moulijn, J.A., Kreutzer, M.T., 2008. Dispersion and holdup in multiphase packed bed microreactors. Chem. Eng. Technol. 31 (8), 1130–1139.

Mazzini, A., Ivanov, M.K., Nermoen, A., Bahr, A., Bohrmann, G., Svensen, H., Planke, S., 2008. Complex plumbing systems in the near subsurface: geometries of authigenic carbonates from Dolgovskoy mound (Black Sea) constrained by analogue experiments. Mar. Petrol. Geol. 25, 457–472.

Mörz, T., Karlik, E.A., Kreiter, S., Kopf, A., 2007. An experimental setup for fluid venting in unconsolidated sediments: new insights to fluid mechanics and structures. Sediment. Geol. 196, 251–267.

Nambiar, D.K.R., Kumar, R., Das, T.R., Gandhi, K.S., 1992. A NEX model for the breakage frequency of drops in turbulent stirred dispersions. Chem. Eng. Sci. 12, 2989–3002.

Nermoen, A., Galland, O., Jettestuen, E., Fristad, K., Podladchikov, Y., Svensen, H., Malthe-Sørenssen, A., 2010. Experimental and analytic modeling of piercement structures. J. Geophys. Res. 115, B10202.

Percy, J.S., Sleicher, C.A., 1983. Drop breakup in the flow of immiscible liquids through an orifice in a pipe. AIChE J. 29 (1), 161–164.

Reddy, K.R., Adams, J.A., 2001. Effects of soil heterogeneity on airflow patterns and hydrocarbon removal during in situ air sparging. J. Geotech. Geoenviron. Eng. 3, 234–247.

Sandnes, B., Flekkøøy, E.G., Knudsen, H.A., Knudsen, H.A., Måløy, K.J., See, H., 2011. Patterns and flow in frictional fluid dynamics. Nat. Commun. 2, 288.

Semer, R., Adams, J.A., Reddy, K.R., 1998. An experimental investigation of air flow patterns in saturated soils during air sparging. Geotech. Geol. Eng. 16, 59–75.

Stankiewicz, A.I., Moulijn, J.A., 2000. Process intensification: transforming chemical engineering. Chem. Eng. Prog. 96 (1), 22–34.

Stemmet, C.P., Bartelds, F., van der Schaaf, J., Kuster, B.F.M., Schouten, J.C., 2008. Influence of liquid viscosity and surface tension on the gas–liquid mass transfer coefficient for solid foam packings in co-current two-phase flow. Chem. Eng. Res. Des. 86, 1094–1106.

Stemmet, C.P., Jongmans, J.N., van der Schaaf, J., Kuster, B.F.M., Schouten, J.C., 2005. Hydrodynamics of gas–liquid counter-current flow in solid foam packings. Chem. Eng. Sci. 60, 6422–6429.

Stemmet, C.P., van der Schaaf, J., Kuster, B.F.M., Schouten, J.C., 2006. Solid foam packings for multiphase reactors—modelling of liquid holdup and mass transfer. Chem. Eng. Res. Des. 84 (A10), 1134–1141.

Tary, J.-B., Géli, L., Henry, P., Sultan, N., Guennou, C., Çağatay, N., Vidal, V., 2012. Micro-events produced by gas migration and expulsion at the seabed: a study based on sea bottom recordings from the sea of Marmara. J. Geophys. Res. 190, 993–1007.

Topin, F., Bonnet, J.-P., Madani, B., Tadrist, L., 2006. Experimental analysis of multiphase flow in metallic foam: flow laws, heat transfer and convective boiling. Adv. Eng. Mater. 8 (9), 890–899.

Tourvielle, J.-N., Philippe, R., de Bellefon, C., 2015. Milli-channel with metal foams under an applied gas–liquid periodic flow: external mass transfer performance and pressure drop. Chem. Eng. J. 267, 332–346.

Tourvielle, J.-N., Philippe, R., de Bellefon, C., 2015. Milli-channel with metal foams under an applied gas–liquid periodic flow: flow patterns, residence time distribution and pulsing properties. Chem. Eng. Sci. 126, 406–426.

Twigg, M.V., Richardson, J.T., 2007. Fundamentals and applications of structured ceramic foam catalysts. Ind. Eng. Chem. Res. 46, 4166–4177.

van Steijn, V., Kreutzer, M.T., Kleijn, C.R., 2007. μ-PIV study of the formation of segmented flow in microfluidic T-junctions. Chem. Eng. Sci. 62, 7505–7514.

Varas, G., Géminard, J.-C., Vidal, V., 2013. Air invasion in a granular layer immersed in a fluid: morphology and dynamics. Gran. Matt. 15, 801–810.

Varas, G., Ramos, G., Géminard, J.-C., Vidal, V., 2015. Flow and fracture in water-saturated, unconstrained granular beds. Front. Phys. 3, 44.

Völkel, N., 2009. Design and Characterization of Gas–Liquid Microreactors Ph.D. thesis. Université de Toulouse, 135.